CrystEngComm

Accepted Manuscript

ROYAL SOCIETY OF CHEMISTRY

www.rsc.org/crystengcomm

Journal Name

RSCPublishing

ARTICLE

Polyhierarchically structured TiP_2O_7/C microparticles with enhanced electrochemical performance for lithium-ion batteries

Yanru Sun[a], Ligang Gai[a]*, Yan Zhou[a], Xinzhu Zuo[b], Jianhua Zhou[a], and Haihui Jiang[a]

Cite this: DOI: 10.1039/xoxxoooooox

Received ooth January 2012,
Accepted ooth January 2012

DOI: 10.1039/xoxxoooooox

www.rsc.org/

Polyanionic compounds with three-dimensional (3D) framework structure have attracted much interest in the role of electrode materials for organic and/or aqueous lithium-ion batteries, due to their relatively high lithium-ion mobility, competitive energy density, good thermal/electrochemical stability, and low cost. In this paper, polyhierarchically structured TiP_2O_7/C microparticles constructed by carbon-coated nanoflakes enchasing crystalline nanoparticles have been prepared by directly annealing flower-like titanium hydrogen phosphate hydrate ($Ti(HPO_4)_2{\cdot}xH_2O$, THPH) microparticles, which are produced with tetrabutyl titanate and phytic acid in an ethanol-thermal medium. A reasonable formation mechanism of the flower-like THPH microparticles is proposed on the basis of time-dependent experimental results and theoretical calculations. The carbon layer plays a crucial role in the formation of TiP_2O_7/C polyhierarchical architecture. When cycled at 1 C for 100 cycles, 2 C for 200 cycles, and 5 C for 400 cycles, the TiP_2O_7/C microparticles exhibit exceptional reversible specific capacities of 128, 123, and 90 mAh g^{-1} with capacity retention being 95.1%, 93.2%, and 94.4%, respectively. The high performance is attributed to interfacial Li-storage and fast Li-ion diffusion due to the polyhierarchical architecture with carbon nano-coating and 3D open pores.

1. Introduction

Controlled synthesis of hierarchically structured nano- and/or micro-materials has been an increasingly hot research topic, because hierarchical structures have widely potential applications in the fields of bionics,[1] thermoelectrics,[2] photocatalysis,[3,4] sensors,[5] solar cells,[3,6] and lithium-ion batteries (LIBs).[3,7-11] The relatively high surface area and sharp corners and edges characteristics of hierarchical structures offer copious active sites for reaction on the surface.[7] Also, multimodal pores formed by self-assembly of building-blocks of the hierarchical structures facilitate mass/charge transfer and provide additional pseudo-capacitive interfacial Li-storage.[8,12]

As a polyanionic compound, titanium pyrophosphate (TiP_2O_7) has a superstructure constructed by TiO_6 and PO_4 polyhedra sharing corners in a three-dimensional (3D) network (Fig. S1†).[13-15] Such a polyanionic framework enables high alkali-ion mobility, high reversible capacity, and good electrochemical/thermal stability.[16-20] In association with the highly reversible Ti^{4+}/Ti^{3+} redox couple, TiP_2O_7 has been subjected to extensive research in catalysis,[21] photocatalysis,[22] hybrid supercapacitor,[23] and LIBs.[10,16-18,23-26] However, the rate performance of pristine TiP_2O_7 was greatly restricted by sluggish kinetics of electron transfer.[27] To improve the electrochemical performance of TiP_2O_7, several strategies have been designed by coating with carbon,[28] doping with metal ions,[29] synthesizing mesoporous structure,[16] and downsizing the particles.[18,23] Although nanoparticles favor to improve electrode performance by means of enlarging surface area and shortening diffusion length for charges, they adversely affect electrolyte stability, electrode packing density, and volumetric energy density.[9,30] To circumvent these issues related to the downsizing strategy, nanoparticles combined with carbon 'nano-painting' have been universally employed as the electrode materials.[11,30] Compared with the nanosized counterparts, microparticles have a more tendency to form close-packed arrays conducive to increase the packing density and volumetric energy density.[9,31] However, there have been no reports on carbon-coated hierarchically structured TiP_2O_7 microparticles and their electrochemical performance.

Phytic acid (PA), i.e. 1,2,3,4,5,6-hexakis(dihydrogen phosphate) *myo*-inositol, and phytates are widely contained in and released by various plant and food materials.[32,33] The investigations relative to PA were mainly focused on using it

for adsorption of metal ions.[33,34] Recently, PA has been employed as an eco-friendly phosphorous source for synthesizing $LiFePO_4$/C nano/microspheres with superior electrochemical performance for LIBs.[35] However, the conductive carbon layer upon $LiFePO_4$ was achieved by additional acetylene (C_2H_2) vapor deposition.[35] Considering that single PA molecule has a six-member carbon ring carrying one $–H_2PO_4$ group at each carbon, we optimized the geometries of PA through theoretical calculations. The calculation results show that both the six $–H_2PO_4$ groups and the PA configuration are approximately located in one plane, probably due to strong hydrogen bonding (S2†).

In view of the interesting molecular structure of PA, we employed it as the phosphorus source, structure-directing agent, and *in situ* carbon source to synthesize carbon-coated TiP_2O_7 (TiP_2O_7/C) with hierarchical architecture and hence high electrochemical performance. The synthetic strategy consists of two steps: (i) scalable synthesis of monodisperse flower-like titanium hydrogen phosphate hydrate ($Ti(HPO_4)_2{\cdot}xH_2O$, THPH); and (ii) polyhierarchical TiP_2O_7/C microparticles constructed by nanoflakes enchasing crystalline nanoparticles obtained by directly annealing THPH without adding any extra organic compound/gas to form the carbon layer. As expected, this novel polyhierarchical architecture exhibits exceptional electrochemical properties for LIBs as compared with previous reports on TiP_2O_7 (Table S2†).[10,16-18,23-25]

2. Experimental

2.1. Preparation of polyhierarchical TiP_2O_7/C microparticles

Phytic acid ($C_6H_6(H_2PO_4)_6$, PA) was purchased from Shanghai Jingchun Industrial Co., China. All chemicals were directly used without further purification. The polyhierarchical TiP_2O_7/C microparticles were prepared by a solvothermal approach combined with annealing treatment. In brief, 3 mmol of tetrabutyl titanate ($Ti(O\textit{n}\text{-}C_4H_9)_4$, TBT) was added into a flask containing 75 mL of anhydrous ethanol with constant stirring to form a clear solution, followed by addition of 1.05 mmol of PA to form a latex. After ultrasonic treatment at room temperature for 5 min, the latex was transferred into a Teflon-lined autoclave with capacity of 95 mL. The autoclave was heated at 190 °C for 12 h, and allowed to cool to room temperature. The precipitate was collected by filtration, washed with distilled water and ethanol several times, and finally dried in a vacuum oven. The obtained powders were determined to be titanium hydrogen phosphate hydrate ($Ti(HPO_4)_2{\cdot}xH_2O$, THPH) (Fig. S3†). To obtain the polyhierarchical TiP_2O_7/C microparticles, the THPH powders were transferred into a tubule furnace, followed by introducing N_2 (150 mL min^{-1}) to purge air in the furnace for 0.5 h, and then annealed in N_2 atmosphere at 750 °C for 4 h, with a heating rate of 2 °C min^{-1}. The resulting product is black in color. The THPH powders were also annealed in air with otherwise identical conditions for comparison, yielding the uncoated TiP_2O_7 counterparts.

2.2. Characterizations

X-ray diffraction (XRD) patterns were recorded on a Bruker D8 Advance diffractometer with Cu Kα radiation (λ = 1.5406 Å), operating at 40 kV and 40 mA. Crystallite sizes (S) of the samples were calculated from the XRD data, according to the Scherrer equation, i.e. $S = 0.9\lambda/\beta\cos\theta_B$, where λ is the X-ray radiation wavelength, β is the full line width at half-maximum height of the corresponding peak after subtraction of the equipment line broadening, and θ_B the Bragg angle. Raman spectra were collected at room temperature on a Renishaw inVia plus laser Raman spectrometer with a 514.5 nm Ar^+ ion laser. Scanning electron microscopy (SEM) images were taken on a Hitachi S-4800 field-emission scanning electron microscope. Transmission electron microscopy (TEM) images and the selected-area electron diffraction (SAED) pattern were taken on a Philips Tecnai Twin-20U high-resolution transmission electron microscope, operating at an accelerating voltage of 200 kV. Fourier transform infrared (FT-IR) spectra were collected on a Shimadzu IRPrestige-21 infrared spectrometer using pressed KBr discs. The FT-IR spectra were recorded with resolution of 4 cm^{-1} over the range of 4000–400 cm^{-1}. Thermogravimetric (TG) and differential scanning calorimetric (DSC) analysis were carried out on a Perkin-Elmer DSC-2C thermogravimetric analyzer, operating at a heating rate of 10 °C min^{-1} in air and nitrogen, respectively.

Nitrogen adsorption/desorption isotherms were collected at 77.5 K using a Micromeritics ASAP 2020 sorption analyzer. The Brunauer–Emmett–Teller (BET) method was utilized to calculate the specific surface areas (S_{BET}). Pore size distributions (PSDs) were determined from adsorption data by the Barrett–Joyner–Halenda (BJH) method. Total volume in pores was calculated from the amount of adsorbed N_2 at a relative pressure ($P/P°$) of 0.97. Micropore area and micropore volume were determined by the *t*-plot method**.** Before recording the nitrogen sorption isotherms, the samples were degassed at 200 °C for 10 h.

2.3. Theoretical calculations

The geometric structures of PA molecule were optimized by the B3LYP method on the basis of density functional theory (DFT) at the 6-31G(d) basis sets. All the calculations were performed with the Gaussian 03 program package.

2.4. Electrochemical tests

Electrochemical properties of the samples were evaluated by assembling CR2032 coin cells. The cells were based on the configuration of Li metal(–)|electrolyte|sample powders(+), using microporous polypropylene film (Celgard 2400) as the cell separator. The electrolyte was 1 M $LiPF_6$ dissolved in ethylene carbonate (EC)/dimethyl carbonate (DMC)/diethyl carbonate (DEC) (1:1:1, v/v/v) solution, purchased from Zhangjiagang Guotai-Huarong New Chemical Materials Co., China. The positive electrode was prepared by blade-coating homogeneously blended slurry onto aluminium foil, and then dried in a vacuum oven at 80 °C for 12 h. The slurry consists of

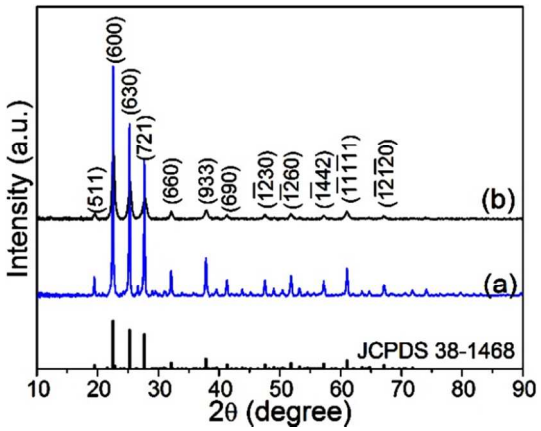

Fig. 1 XRD patterns of TiP_2O_7 (a) and TiP_2O_7/C (b).

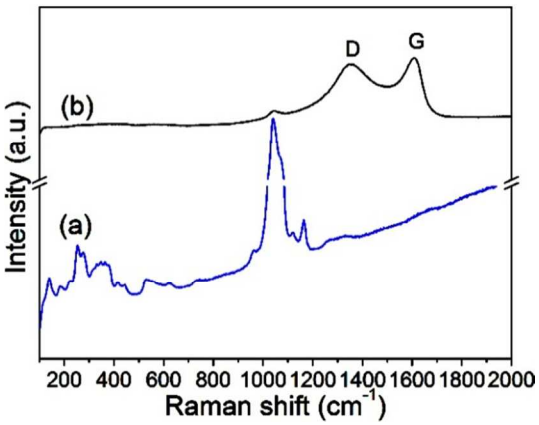

Fig. 2 Raman spectra of TiP_2O_7 (a) and TiP_2O_7/C (b).

70 wt.% active material, 20 wt.% acetylene black, and 10 wt.% polyvinylidene fluoride (PVDF) in *N*-methylpyrrolidone. The aluminium foil with dried coating was subjected to double rolling to make a smooth surface, and then cut into circular sheets with diameter of 12 mm. The mass of active material of single electrode was in the range of 2–3 mg. The assembly of cells was completed in an Ar-filled glove box, in which oxygen and moisture were kept below 5 ppm.

Cyclic voltammetry curves were measured in a potential range of 1.5–3.5 V at a scan rate of 0.1 mV s^{-1}, using a CHI 660E electrochemical workstation (Shanghai CH Instruments Co., China). Galvanostatic charge/discharge measurements were carried out at 0.1–10 C with voltage range of 1.5–3.5 V (vs. Li^+/Li), using a LANHE CT2001A battery tester (Wuhan LANHE Co., China). The specific capacity for the composite sample was calculated with including the weight of the carbon component. Alternating current (AC) electrochemical impedance spectroscopy (EIS) measurements were performed at the open circuit voltage in a frequency range of 10^{-2}–10^5 Hz, with AC amplitude of 5 mV.

3. Results and discussion

3.1. Structure, composition, and morphology

Fig. 1 shows the XRD patterns of the samples. Both of the samples annealed in air (Fig. 1a) and in nitrogen (Fig. 1b) with cell parameter *a* equaling to 2.365 nm can be indexed to cubic TiP_2O_7 with *P*a3 space group and 3 × 3 × 3 superstructure (JCPDS no. 38-1468), consistent with the previous report on crystalline TiP_2O_7.[25] Compared with Fig. 1a, all the diffraction peaks in Fig. 1b are relatively lower in intensity, due to the effect of carbon that retards the phase transformation of THPH and then restricts the growth of TiP_2O_7 crystallites (Fig. S4†). The carbon is derived from the adsorbed *myo*-inositol and inositol phosphates (IPs) upon THPH, due to the strong hydrogen bonding between THPH and *myo*-inositol/IPs, which are transformed from PA in a solvothermal environment.[36] According to the Scherrer formula using the data of (600), (630), and (721) planes, the mean crystallite size of TiP_2O_7/C is 20.7 nm, smaller than that of 39.7 nm for TiP_2O_7. This result indicates that both of the samples contain primary nanoparticles, in accordance with the electron microscopy observations (Figs. 4 and 5).

To further differentiate the two samples, Raman spectra were collected at room temperature. The observed Raman bands in Fig. 2a are consistent with the previous reports on TiP_2O_7.[15,37] The strong band centered at 1041 cm^{-1} and the shoulder band around 1070 cm^{-1} are assigned to $\nu_s(PO_3)$ symmetric stretching vibration mode.[15,37] The weak bands centered at 1164 and 1120 cm^{-1} are assigned to $\nu_{as}(PO_3)$ asymmetric stretching mode.[37] The small bands at 960 and 735 cm^{-1} correspond separately to ν_{as}(POP) and ν_s(POP) stretching vibrations.[37] In addition, seven weak bands occur at low wavenumbers around 530, 443, 414, 363, 346, 275, and 253 cm^{-1}. The former three and the latter four bands are attributed to $\delta(PO_3)$ and δ(POP) bending vibrations,[15,37] respectively. The small band around 623 cm^{-1} is assigned to $\nu_1(TiO_6)$ mode.[37] This assignment is based on the fact that TiP_2O_7 consists of TiO_6 octahedra and PO_4 tetrahedra alternatively linked to form chains.[13-15] In a similar way, the band at 140 cm^{-1} can be assigned to $\nu_6(TiO_6)$ mode. For the TiP_2O_7/C sample (Fig. 2b), most of the bands related to TiP_2O_7 are sheltered by carbon coating, apart from the band at 1041 cm^{-1} characteristic of $\nu_s(PO_3)$. This result indicates that carbon in the composite sample is coated upon rather than blended with TiP_2O_7 particles. The existence of carbon layer is revealed by two broad bands centered at 1353 and 1608 cm^{-1}. The former is related to disordered carbon (D band), and the latter corresponds to the G (graphitic) band with optically allowed E_{2g} vibrations of the graphitic structure.[38] The peak intensity ratio between the D and G bands (I_D/I_G) is indicative of the degree of crystallinity of the carbon, i.e., the smaller the I_D/I_G ratio, the higher the ordering degree of the carbon material.[39,40] In the present case, the I_D/I_G ratio is ca. 0.96, demonstrating that the carbon upon TiP_2O_7 particles is partially graphitic. This facilitates to improve the kinetics of electron transfer and hence the rate performance of electrode using TiP_2O_7/C as the active

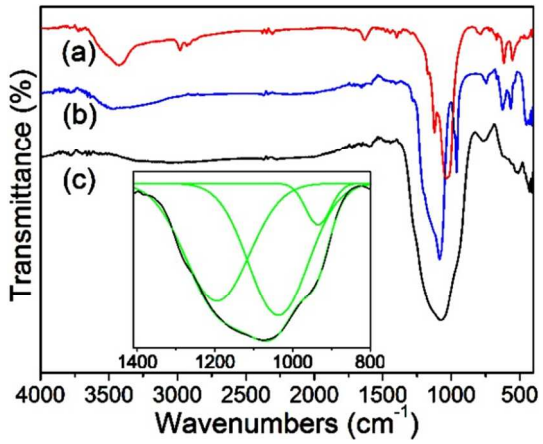

Fig. 3 FT-IR spectra of THPH (a), TiP_2O_7 (b), and TiP_2O_7/C (c).

material.

FT-IR technique was employed to examine surface chemistry of the samples. In the THPH spectrum (Fig. 3a), the peaks centered at 3423 and 1630 cm^{-1} correspond separately to ν(O–H) stretching and δ(O–H) bending vibrations, due to the surface-adsorbed water, *myo*-inositol/IPs, and the hydrate water in THPH. The presence of *myo*-inositol and IPs upon THPH are confirmed by the peaks corresponding to ν(C–H) (2982 and 2923 cm^{-1}), δ(C–H) (1396 cm^{-1}), ν(C–OP) (1123 cm^{-1}),[41] and γ(C–H) (785 and 668 cm^{-1}) vibrations, which also occur in the IR spectrum of *myo*-inositol with analytical grade (Fig. S5b†). The peaks at 1033, 613, and 551 cm^{-1} corresponding separately to ν(P–O), ν_{as}(O–P–O), and ν_s(O–P–O) stretching vibrations[15,16,21] are due to the HPO_4 groups of THPH/IPs.[15]

In Fig. 3b, aside from the broad peak around 3430 cm^{-1} due to surface-adsorbed water, the other peaks (1084, 961, 747, 623, and 564 cm^{-1}) are characteristic of TiP_2O_7.[16,21] The peaks at 961 and 747 cm^{-1} are separately assigned to ν_{as}(P–O–P) and ν_s(P–O–P) vibrations.[16,21] Compared with those in Fig. 3a, the peaks corresponding to ν(P–O) in terminal PO_3 (1084 cm^{-1}),[42] ν_{as}(O–P–O) (747 cm^{-1}), and ν_s(O–P–O) (623 cm^{-1}) blue-shift to high wavenumbers. This result arises from the reduction in P–O bond length, due to the transformation of two HPO_4 groups into one P_2O_7 group.[21] As for the TiP_2O_7/C spectrum (Fig. 3c), there are three weak peaks corresponding to ν(C=C) (1590 and 1445 cm^{-1}) in graphitic carbon ring[43] and γ(C–H) (765 cm^{-1}) out-of-plane bending vibrations, respectively. However, the peaks characteristic of ν(P–O–P) and ν(O–P–O) are absent due to carbon coating, leaving a broad and strong peak centered at 1071 cm^{-1}. This peak can be fitted with Gaussian functions into three peaks at 1195, 1037, and 934 cm^{-1} (Fig. 3, inset), corresponding separately to ν(C–OP) (46.1%),[41] ν(P–O) in terminal PO_3 (47.7%),[42] and ν_{as}(P–O–P) (6.2%) in pyrophosphate.[16,21] On the basis of the FT-IR and Raman results, we conclude that the *myo*-inositol/IPs upon THPH act as the *in situ* carbon source, and finally turn into partially graphitic carbon layer upon TiP_2O_7 after annealing treatment in nitrogen. This is confirmed by the SEM mapping images of

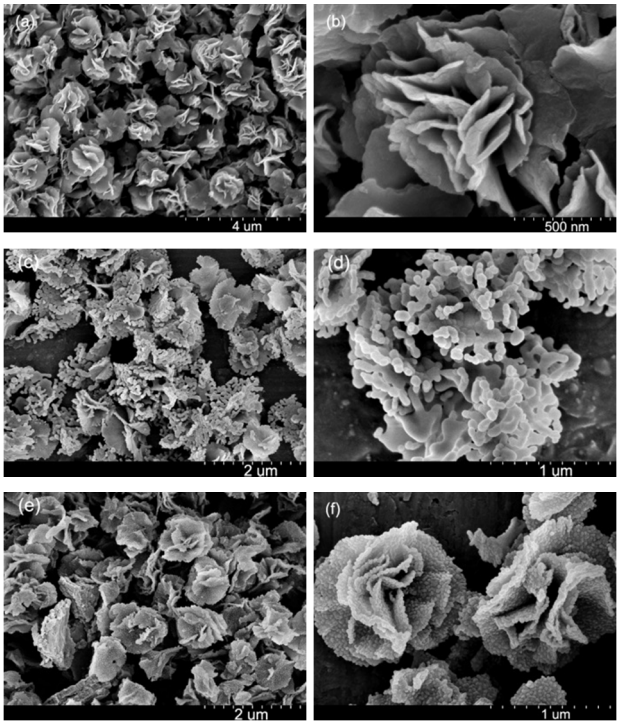

Fig. 4 SEM images of THPH (a, b), TiP_2O_7 (c, d), and TiP_2O_7/C (e, f).

TiP_2O_7/C (Fig. S6†), where carbon is uniformly distributed upon the sample.

Fig. 4 shows the SEM images of the samples. It is apparent that the THPH sample is mainly composed of flower-like microparticles with size ranging from 1.1 to 1.35 μm (Fig. 4a and b). SEM mapping images of THPH (Fig. S7†) reveal uniform distribution of C arising from surface-adsorbed *myo*-inositol/IPs compounds, in concert with the FT-IR spectrum (Fig. 3a). The individual microflower is constructed by nanoflakes with relatively smooth surface. The thickness of nanoflakes is in the range of 20–50 nm. After annealing treatment in air, many microflowers are broken (Fig. 4c), producing crumpled nanoflakes rimmed with or constituted by nanoparticles with size in the range of 40–100 nm. (Fig. 4d). This phenomenon is caused by the weakened interactions between the nanoflakes, probably due to (i) dehydration of THPH to accomplish phase transformation; (ii) gas release from decomposition of the adsorbed organic compounds upon THPH; and (iii) coarsening of the formed TiP_2O_7 crystallites. However, most of the microparticles retain the flower-like structure after annealing treatment in nitrogen (Fig. 4e). More significantly, the nanoflakes constituting microflowers are not broken but enchased with quasi-spherical nanoparticles with size in the range of 20–40 nm. The nanoparticles distributed upon nanoflakes produce interconnected interspaces with size less than 25 nm between adjacent grains (Fig. 4f).

On the basis of the XRD/Raman/SEM results, we conclude that the formation of carbon layer upon TiP_2O_7

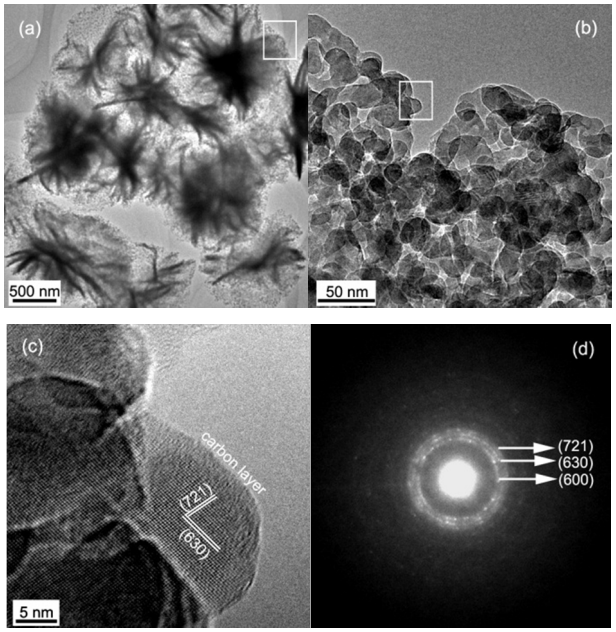

Fig. 5 (a) Low-magnification TEM image of TiP_2O_7/C; (b) High-magnification image corresponding to the squared area in a; (c) High-resolution image corresponding to the squared area in b; and (d) SAED pattern corresponding to a.

nanoparticles contributes to form the 3D polyhierarchical architecture with open pores through retarding the phase transformation of THPH and inhibiting the coarsening of TiP_2O_7 crystallites, in concert with the TG/DSC (Fig. S4†) and XRD results (Fig. 1).

This novel structure of the composite sample is also confirmed by the TEM images (Fig. 5a–c). The nanoparticles with size range of 20–40 nm and nanopores with size less than 4 nm are clearly observed (Fig. 5a and b). The nanopores are created between adjacent nanoparticles residing on nanoflakes. The phase of the nanoparticles is determined by the SAED pattern (Fig. 5d), in which the diffraction rings from inner to outer correspond to (600), (630), and (721) planes of cubic TiP_2O_7 (JCPDS no. 38-1468). Furthermore, the degree of crystallinity of the nanoparticles is revealed to be nearly single-crystalline, based on the high-resolution two-dimensional (2D) lattice fringe image with spacing of ca. 0.35 and 0.32 nm corresponding separately to d_{630} and d_{721} of cubic TiP_2O_7 (Fig. 5c). Also, the carbon layer with thickness of 2–3 nm can be discerned from the edge of the examined nanoparticle, where the lattice fringes stop at the interface between the substrate and surface layer (Fig. 5c).[37,44] The content of carbon in the composite sample is ca. 2.48 wt% calculated from the data of TG (Fig. S4†). It has been demonstrated that even a small amount of carbon (less than 1 wt%) in $LiFePO_4$/C composite produces a significant increase in rate capability, but unfortunately, a dramatic decrease in tap density.[45] The tap density of TiP_2O_7/C is 0.64 g cm^{-3}, which is only slightly reduced compared with that of 0.67 g cm^{-3} for TiP_2O_7. This is attributed to the thin layer of carbon, through which Li ions can pass from the electrolyte into the solid TiP_2O_7 where they are stored, while the carbon layer provides electrons near

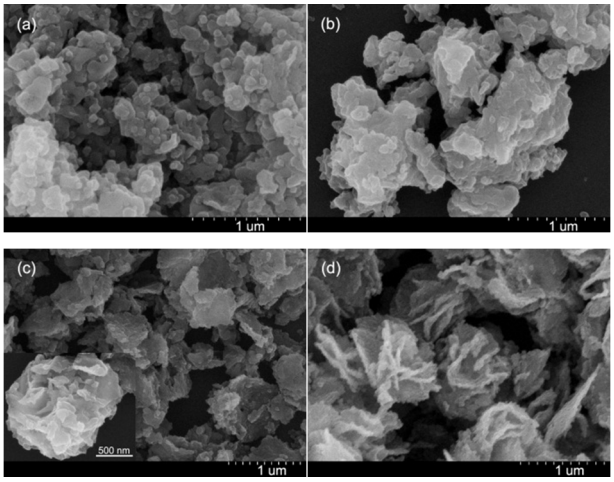

Fig. 6 SEM images of THPH samples prepared at 190 °C fro: (a) 3 h; (b) 6 h; (c) 7.5 h; and (d) 9 h.

the spots of Li-ion insertion to satisfy the electroneutrality of the active material. Therefore, it can be expected that TiP_2O_7/C will show enhanced electrochemical properties due to the thin layer carbon-coated 3D polyhierarchical architecture without dramatic loss of tap density.

3.2. Formation mechanism of the flower-like architecture

To understand the formation mechanism of flower-like microparticles, the SEM images of THPH synthesized as a function of the reaction time are presented in Fig. 6. When the reaction time is 3 h, the sample mainly consists of primary particles with size ranging from 30 to 220 nm (Fig. 6a). The primary particles tend to form agglomerates. With increasing the reaction time to 6 h, submicro- and microparticles dominate the sample (Fig. 6b), probably due to the van der Waals attraction and the well-known Ostwald ripening mechanism.[46] As the reaction time increases to 7.5 h, nanoflakes peel off the microparticles (Fig. 6c, inset), producing the sample composed of nanoflakes with thickness in the range of 20–50 nm (Fig. 6c). The samples prepared at the time range of 6–12 h are determined to be THPH ($Ti(HPO_4)_2{\cdot}xH_2O$) (Fig. S3†), where x = 1.24 for the sample obtained at 12 h (S5†). As demonstrated in literature,[47] the structure of THPH is built up of layers of slightly distorted TiO_6 octahedra and alternating HPO_4 tetrahedra. The layers bound only by van der Waals forces have a pseudo-hexagonal symmetry and stack along the c-axis.[47] Therefore, the formation of nanoflakes is due to interlaminar dissociation of THPH. However, nanoflakes and microflowers cannot be obtained by using H_3PO_4 (85 wt%) as the phosphorous source under otherwise identical reaction conditions (Fig. S8†), indicating that PA plays a crucial role in the formation of nanoflakes.

As mentioned before, single PA molecule carries six $–H_2PO_4$ groups approximately in one plane (Fig. S2†). The approximately planar configuration matches the layered structure of THPH. In the initial stage, the $–H_2PO_4$ groups of PA strongly interact with titanium ions of titanate through coordination (Scheme 1a),[33,34] producing an amorphous product

at 3 h (Fig. S3a†). Phosphate groups tend to be released step by step from the six-member carbon ring in a solvothermal environment, resulting in the formation of *myo*-inositol and IPs.[36] It is believed that partial $–H_2PO_4$ groups remain on the

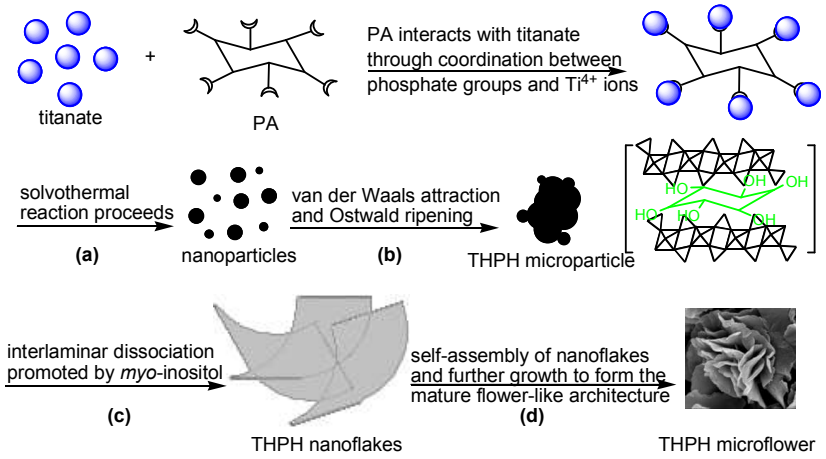

Scheme 1 Illustration of the formation mechanism of flower-like architecture. The crescents in phytic acid molecule denote $–H_2PO_4$ groups. The tetragonal pyramids and triangles in the square bracket denote TO_6 octahedra and HPO_4 tetrahedra, respectively.

Table 1 BET specific surface area (S_{BET}) and pore parameters of the samples.

Sample	S_{BET} ($m^2\ g^{-1}$)	Total pore volume ($cm^3\ g^{-1}$)	Total pore area ($m^2\ g^{-1}$)	Micropore volume ($cm^3\ g^{-1}$)	Micropore area ($m^2\ g^{-1}$)	Average pore width (nm)	S_{micro}/S_{BET} (%)
TiP_2O_7	45.4	0.13	26.1	0.0024	6.1	12.1	13.4
TiP_2O_7/C	40.4	0.11	19.8	0.0049	11.0	12.9	27.2

the carbon framework and concurrently interact with titanium ions at this stage. This suggestion is partially supported by the result of high performance liquid chromatography (HPLC) measurements to examine the time-dependent molar ratio of *myo*-inositol/IPs in reaction media (Fig. S9†). The molar ratio gradually increases with increasing the reaction time, and tends to level off with the reaction time above 7.5 h. At this time, nanoflakes emerge in multitude (Fig. 6c). Therefore, we speculate that phosphate groups detach from the carbon framework and combine with titanate to form THPH in the time range of 3–6 h, leaving some *myo*-inositol molecules staying in interlayer of the THPH structure (Scheme 1b). By examining the cell parameter *c* of α-THPH, this speculation is confirmed by the fact that the cell parameter *c* for the sample prepared with PA for 6 h (Fig. S3b†) is 15.3468 Å, larger than that of 15.0978 Å for the sample prepared with H_3PO_4 under otherwise identical reaction conditions (Fig. S3f†). This result indicates that the *myo*-inositol molecules inside the interlayers reduce interactions between the layers stacked along the *c*-axis. This facilitates interlaminar dissociation of THPH to form nanoflakes at 7.5 h (Scheme 1c). At the same time, the *myo*-inositol molecules originally staying in interlayers are released into the reaction medium, yielding the molar ratio of *myo*-inositol/IPs approaching maximum (Fig. S9†). As the solvothermal reaction proceeds, the nanoflakes with high specific surface area tend to rotate and approach each other to eliminate high surface energy by diminishing dangling bonds,[48] leading to the formation of self-assembled flower-like microparticles in an embryonic form (Fig. 6d).[49] Further growth of the embryonic flower-like architecture is presumably continued by surface diffusion and feedstock supplied to the rim of nanoflakes,[50] and finally producing the mature flower-like architecture (Scheme 1d).

3.3. S_{BET} and pore structures

Fig. 7 shows the adsorption/desorption isotherms and the corresponding pore size distribution (PSD) curves of TiP_2O_7 and TiP_2O_7/C. Both of the convolution curves belong to type-IV isotherm with type-H3 hysteresis loop according to BDDT classification,[51] indicating the presence of mesopores (2–50 nm) in the two samples.[52] Moreover, the observed hysteresis loops occurring at high relative pressure ($P/P°$) regions (0.8–1.0) suggest the presence of macropores (>50 nm).[52] The PSD curves (Fig. 7, inset) exhibit a bimodal characteristic with pore size concentrated on 1.7 and 10.6 nm, along with a wide pore-size range from 1.7 to over 60 nm. The textural parameters derived from the isotherms are summarized in Table 1. The total pore volume and total pore area of TiP_2O_7/C are lower than those of TiP_2O_7 (Table 1), resulting in a relatively lower S_{BET} for the composite sample. The decrease in S_{BET} is due to the carbon coating that prevents the flower-like structures from fragmenting into nanoparticles (Fig. 4e and f).It should be pointed out that the ratio S_{micro}/S_{BET} (27.2%) for TiP_2O_7/C is almost twice of that (13.4%) for TiP_2O_7, indicating that the micropores (1.7–2 nm) contribute more to TiP_2O_7/C as compared with TiP_2O_7. The increase in micropores for the

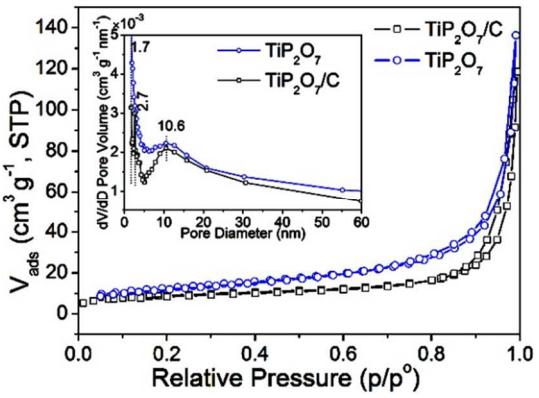

Fig. 7 Nitrogen adsorption/desorption isotherms of the samples and the corresponding pore size distribution curves (inset).

composite sample is attributed to the polyhierarchical architecture where micrometer-sized voids are created by TiP_2O_7 nanoparticles upon nanoflakes, as observed in Fig. 5b. The bimodal porosity of the samples containing micropores and mesopores/macropores is beneficial to improve the rate performance and specific capacity, because the pores serving as electrolyte container not only facilitate fast diffusion of Li ions to and from the lattice of TiP_2O_7,[9,11,35,44] but also allow additional interfacial Li-storage through charge separation.[8,12]

On the basis of the above analysis, the polyhierarchically structured TiP_2O_7/C microparticles present a promising electrode material for LIBs, based on the features with well-crystalline nanoparticles upon nanoflakes, moderate S_{BET}, bimodal porosity, and thin layer of partially graphitic carbon coating. The microparticles and thin layer of carbon enable relatively denser packing beneficial for the volumetric capacity, and the carbon-coated nanoflakes enchasing crystalline nanoparticles as well as the porous structure favor improved specific capacity and rate capability.

3.4. Electrochemical properties

The potential application of polyhierarchically structured TiP_2O_7/C was examined in the role of Li insertion/extraction. The lithium-storage performance of hierarchically structured TiP_2O_7 was also evaluated for comparison. The insertion/extraction of lithium ions with respect to TiP_2O_7 occurs according to equation (1):[23,24]

$$TiP_2O_7 + xLi^+ + xe^- = Li_x(Ti_{1-x}^{4+}Ti_x^{3+})P_2O_7 \ (x \le 1) \quad (1)$$

As demonstrated in literature,[24] the typical discharge curve of TiP_2O_7 crystals has two plateau regions corresponding to galvanostatic discharge curves of TiP_2O_7/C (Fig. 8a) and TiP_2O_7 (Fig. S10a†) samples cycled at different current rates exhibit a sloping characteristic without flat plateau. This characteristic is different from that of TiP_2O_7 nano- and/or microcrystals,[16,24,25] but similar to that of mesoporous TiP_2O_7[16] and TiP_2O_7 nanoplates,[18] and can be assigned to consecutive lithium insertion due to extension of the solid solution domains.[16] Through *in situ* high-resolution TEM observation on nanostructured $LiFePO_4$, J. Li *et al* found a quickly formed Li-sublattice disordered solid solution zone (SSZ), and suggested the SSZ is important as it provides out-of-equilibrium but atomically wide avenues for Li^+/e^- transport.[53] Also, the solid solution domains extend as the crystallite size decreases, leading to increase in discharge region and hence enhancement in discharge capacity.[54] In the present two samples with hierarchical structure, the building blocks of nanoflakes and nanoparticles are responsible for the extension of the solid solution domains.

Fig. 8b shows the galvanostatic charge/discharge curves of TiP_2O_7/C cycled at 1 C (completing the charge or discharge process in 1 h). The discharge specific capacity gradually increases to 134 mAh g^{-1} at the 5th cycle and slowly decreases to 132 mAh g^{-1} at the 25th cycle from the initial capacity of 127 mAh g^{-1}, and then stabilizes at about 128 mAh g^{-1}, which is slightly higher than the theoretical capacity of the active material. In view of 2.48 wt% carbon in the composite sample, the theoretical capacity of the active material is calculated to be 127 mAh g^{-1}, based on the theoretical capacity of 121 and 372 mAh g^{-1} for TiP_2O_7[16] and graphitic carbon.[55] The gradually increasing capacity within the initial several cycles is consistent with the gradually increasing anodic/cathodic current in the initial cyclic voltammograms (Fig. S10b†). This phenomenon often occurs in transition-metal phosphates,[35,56] and can be mainly attributed to a progressively increased active surface area for electrochemical reaction as a result of gradual penetration of electrolyte into the interior of active material.[56] Also, the charge/discharge curves of TiP_2O_7/C show a much overlapped tendency after the first cycle compared with those of bare TiP_2O_7 (Fig. S10c†). This indicates that a stable solid-electrolyte interface (SEI) film formed on the surface/interface of carbon layer in the first cycle can prevent direct contact of encapsulated TiP_2O_7 with electrolyte and safeguard the structural integrity of interior TiP_2O_7 during subsequent cycles, thus leading to high Coulombic efficiency (~100%) and superior reversibility of the sample.[57] The visible shift to high potential of the discharge curves after the first cycle indicates a decreased resistance regarding the reduction of Ti^{4+} in TiP_2O_7, and the slight shift to high potential of the charge process is assigned to polarization.[58] The result that the discharge capacity exceeds the theoretical capacity has been widely reported on transition-metal oxides.[8,55,59] This can be assigned to interfacial Li-storage (discussion below)[8] or the formation of SEI film associated with electrolyte decomposition.[55,59]

Another excellent property of TiP_2O_7/C is the superior rate performance in terms of high capacity retention and reversibility (Fig. 8c and Table S2†). Although TiP_2O_7 also exhibits good cycling stability at current rates ranging from 0.1 to 1 C (Fig. S10d†), the rate performance and the discharge capacity at higher rates (≥ 0.5 C) are inferior to those of the composite sample. In fact, the TiP_2O_7 sample presented here show superior electrochemical performance to the previously reported TiP_2O_7 counterparts (Table S2†).[16,18,23,24]

Journal Name RSCPublishing

ARTICLE

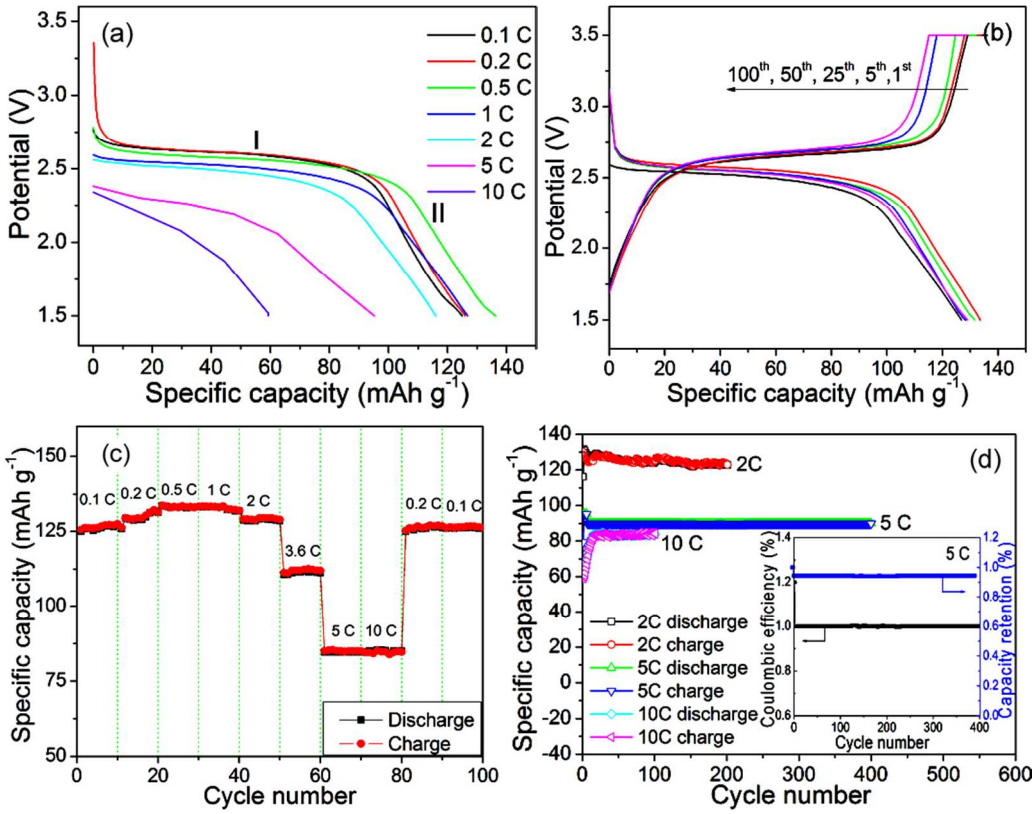

Fig. 8 Electrochemical performance of the TiP_2O_7/C sample: (a) initial discharge curves at various rates; (b) charge/discharge curves cycled at 1 C; (c) charge/discharge capacities at different current rates; and (d) cycling performance at 2 C, 5 C, and 10 C; inset is the capacity retention and Coulombic efficiency at 5 C.

The discharge capacity of TiP_2O_7/C cycled at 2 C for 200 cycles retains 123 mAh g^{-1}, accompanying with capacity retention and Coulombic efficiency (calculated from the discharge capacity/charge capacity) being 93.2% and approaching 100%, respectively (Fig. 8d). Even cycled at 5 C for 400 cycles and 10 C for 100 cycles, the composite sample retains 90 and 84 mAh g^{-1} in discharge capacity, 94.4% and 98.4% for capacity retention, and 100% for Coulombic efficiency, respectively (Fig. 8d). For comparison, the electrochemical performance of TiP_2O_7/C nanoparticle aggregates, which were obtained by annealing the THPH precursor synthesized at 190 °C for 3 h (Fig. 6a and S11†), was also tested as shown in Fig. S10e†. Although the Coulombic efficiency of TiP_2O_7/C nanoparticle aggregates approaches 100%, the discharge capacity after 200 cycles at 2 C, 400 cycles at 5 C, and 100 cycles at 10 C retains only 102, 49.4, and 26.7 mAh g^{-1}, respectively, much lower than the corresponding value of polyhierarchically structured TiP_2O_7/C microparticles.

It should be pointed out that all the electrochemical results discussed refer to the stable performance obtained after several initial cycles. The cycling performance with respect to TiP_2O_7 carried out at higher rates (≥ 2 C) has not been reported in literature (Table S2†). The 2 C-performance regarding the TiP_2O_7/C sample is comparable with that of $LiFePO_4$/C composites cycled at 1.5 C[56] and 1 C,[9,35] presenting a promising electrode material for LIBs.

To understand the enhanced electrochemical performance of TiP_2O_7/C, we should focus on the initial discharge curves collected at various rates (Fig. 8a). The discharge curves are featured with a pseudo-plateau (region I) and a sluggish slope (region II), different from the abrupt slope reported on the typical discharge curves of TiP_2O_7 microparticles.[24] Moreover, the specific capacity at 0.5 C and 1 C is higher than that at 0.1 C. This characteristic is retained after 50 cycles (Fig. S10f†). This phenomenon has been discussed in detail for porous transition metal oxide,[8] and is attributed to interfacial Li-storage.

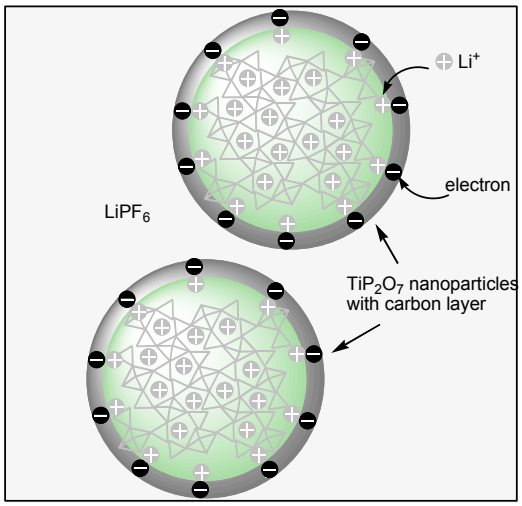

Fig. 9 Illustration of the interfacial Li-storage mechanism for TiP_2O_7/C.

Table 2 Impedance parameters of the samples.

Sample	R_e (Ω)	R_{ct} (Ω)	σ_w (Ω cm^2 s$^{-0.5}$)	D_{Li} (cm^2 s^{-1})
TiP_2O_7	20.3	474.2	889.5	6.2×10^{-14}
TiP_2O_7/C	25.5	267.5	231.5	9.2×10^{-13}

The capacity contributed from the interfacial Li-storage accounts for about 45% total discharge capacity at higher rates (≥ 0.5 C). According to the 'Job-sharing' model,[12] Li^+ ions are stored on the ion-conducting side of the interface, while electrons (e^-) are localized on the electron-conducting side. This can provide additional Li-storage by means of charge separation.[12] In the present case, we suggest that the TiP_2O_7 encapsulated into the carbon acts as the ion-conducting side, whereas the partially graphic carbon layer and the conductive acetylene black act as the electron-conducting part (Fig. 9). Taking interfacial Li-storage at 5 C (40.5 mAh g^{-1}) as an example, the interfacial Li-content can be calculated to be 7.19×10^{-5} mol m^{-2}, based on the suggestion that the interface area approximates the total pore area (19.8 m^2 g^{-1}, Table 1), since the pores arising from grain spacing (less than 25 nm) dominates the pore size distribution of the composite sample (Fig. 7 inset). The calculated interfacial Li-content value is the same in order of magnitude as that in previous reports focused on the interfacial Li-storage mechanism,[8,55,60] indicating a monolayer of the Li-content.[60]

Alternating current (AC) electrochemical impedance spectroscopy (EIS) is a powerful technique to determine the relationship between electrochemical performance and electrode kinetics.[57] Fig. 10a shows the Nyquist plots of fresh coin cells made from TiP_2O_7 and TiP_2O_7/C. They share a common feature with a depressed semicircle at high-to-middle frequency range followed by an inclined line in the low-frequency region. The intercept on the realistic axis (Z_{re}) at the high-frequency end is the electrolyte resistance (R_e), the

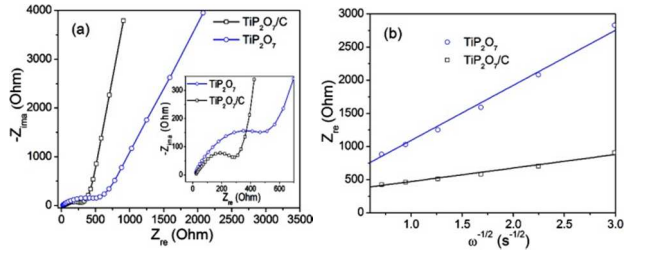

Fig. 10 (a) EIS spectra of the electrodes in the frequency range from 0.01 Hz to 100 KHz; (b) Plots of Z_{re} versus $\omega^{-0.5}$.

diameter of semicircle is indicative of charge-transfer resistance (R_{ct}) associated with the SEI film, and the inclined line represents the Warburg impedance (Z_w) related to the diffusion of lithium ions into the bulk of electrode material.[57,61] It is apparent that the diameter of the semicircle for TiP_2O_7/C is much smaller than that for bare TiP_2O_7, indicating that the electrode made from TiP_2O_7/C possesses lower contact and charge-transfer impedance (Table 2). This facilitates rapid charge transfer during the electrochemical lithium insertion/extraction reaction and thus results in significant enhancement on the rate performance of the composite sample. Also, the inclined line for TiP_2O_7/C approaches nearer to the imaginary axis compared with that for TiP_2O_7, indicating a higher Li-ion diffusion rate for the composite sample. The Li-ion diffusion rate (D_{Li}) can be calculated from equation (2):[62]

$$D_{Li} = R^2T^2/2A^2n^4F^4C^2\sigma_w^2 \quad (2)$$

where R is the gas constant (8.314 J mol^{-1} K^{-1}), T the absolute temperature (298.15 K), F the Faraday constant (96,485 C mol^{-1}), A the surface area of electrode, n the number of electrons transferred per molecule during intercalation, C the molar concentration of Li-ions in TiP_2O_7, and σ_w is the Warburg coefficient which obeys the following relationship (equation (3)):

$$Z_{re} = R_e + R_{ct} + \sigma_w\omega^{-0.5} \quad (3)$$

where Z_{re}, R_e, and R_{ct} have been mentioned above, and ω is the angular frequency $2\pi f$ with f being in the low-frequency range of Nyquist plot. Since both R_e and R_{ct} are kinetics parameters independent of frequency, σ_w is hence the slope of the plot for Z_{re} versus the reciprocal root square of angular frequency ($\omega^{-0.5}$) (Fig. 10b). The σ_w and D_{Li} values for TiP_2O_7 and TiP_2O_7/C are listed in Table 2. It is apparent that the σ_w value for TiP_2O_7/C is much smaller than that for TiP_2O_7. As a result, the D_{Li} value for TiP_2O_7/C is ca. 15 times that for TiP_2O_7. This result gives direct evidence that the polyhierarchical architecture of TiP_2O_7/C with thin layer of partially graphitic carbon and 3D open pores distinctly promotes the charge transfer during the electrochemical reactions, resulting in a significant enhancement in rate performance.

On the basis of the above analysis, the polyhierarchically structured TiP_2O_7/C microparticles show enhanced electrochemical properties including fine specific capacity,

good cycling stability, and especially high rate capability, which have not been demonstrated in previous reports with respect to TiP_2O_7. These properties can be attributed to the following factors: (1) the building blocks of TiP_2O_7 nanoflakes and nanoparticles in the TiP_2O_7/C microparticles shorten the diffusion length for Li ions and hence reduce the time needed for Li ions to migrate into the TiP_2O_7 lattices; (2) the thin layer of partially graphitic carbon upon crystalline TiP_2O_7 not only allow rapid penetration of Li ions in the electrolyte to and from the TiP_2O_7 lattices,[35,44] but also effectively enhances the electronic conductivity and fasten the transport of electrons;[44] and (3) the micropores and mesopores functioning like electrolyte containers facilitate rapid mass/charge transfer and, more significantly, offer enough surface/interface area for additional interfacial Li-storage.[8,56,60]

4. Conclusions

Flower-like TiP_2O_7/C microparticles with polyhierarchical architecture have been prepared by using phytic acid as the phosphorous source, structure-directing agent, and *in situ* carbon source. This polyhierarchical architecture is featured with TiP_2O_7 microparticles constructed by nanoflakes enchasing crystalline nanoparticles. The formation mechanism of the flower-like structure is attributed to self-assembly of nanoflakes resulting from exfoliation of layer-structured titanium hydrogen phosphate hydrate promoted by phytic acid, based on the time-dependent experimental results and theoretical calculations. The carbon layer plays a crucial role in the formation of polyhierarchical architecture of TiP_2O_7/C on the basis of the XRD and TG/DSC results. The as-obtained TiP_2O_7/C hierarchical microparticles exhibit enhanced reversible specific capacities of 128, 123, and 90 mAh g^{-1} when cycled at 1 C for 100 cycles, 2 C for 200 cycles, and 5 C for 400 cycles, superior to individual TiP_2O_7 and nano-aggregated TiP_2O_7/C. The enhanced electrochemical performance is relevant to interfacial Li-storage due to the polyhierarchical architecture with carbon nano-coating and 3D open pores. The unique architecture enables TiP_2O_7/C to be a promising candidate of electrode material for lithium-ion batteries.

Acknowledgements

This research was financially supported by NSFC (no. 51272143).

Notes and references

[a]*School of Chemistry and Pharmaceutical Engineering, Qilu University of Technology, Jinan 250353, People's Republic of China*
[b]*School of Material Science & Engineering, Qilu University of Technology, Jinan 250353, People's Republic of China*

† Electronic Supplementary Information (ESI) available: Schematic illustration of TiP_2O_7 structure, theoretical calculation results, XRD patterns of the THPH samples, TG/DSC analysis of THPH, FT-IR spectra of THPH and myo-inositol, SEM images of THPH prepared with H_3PO_4, HPLC analysis, and supplementary electrochemical performance of TiP_2O_7 and TiP_2O_7/C. See DOI: 10.1039/b000000x/

1 Y. Zhang, Y. Chen, L. Shi, J. Li and Z. Guo, *J. Mater. Chem.,* 2012, **22**, 799–815.
2 K. Biswas, J. He, I. D. Blum, C. I. Wu, T. P. Hogan, D. N. Seidman, V. P. Dravid and M. G. Kanatzidis, *Nature*, 2012, **489**, 414–418.
3 Y. Li, Z. Y. Fu and B. L. Su, *Adv. Funct. Mater.*, 2012, **22**, 4634–4667.
4 Q. C. Liu, D. K. Ma, Y. Y. Hu, Y. W. Zeng and S. M. Huang, *ACS Appl. Mater. Interfaces*, 2013, **5**, 11927–11934.
5 H. Jiang, L. Zhao, L. Gai, L. Ma, Y. Ma and M. Li, *CrystEngComm*, 2013, **15**, 7003–7009.
6 T. P. Chou, Q. Zhang, G. E. Fryxell and G. Cao, Adv. Mater., 2007, **19**, 2588–2592.
7 Z. Sun, J. H. Kim, Y. Zhao, F. Bijarbooneh, V. Malgras, Y. Lee, Y. M. Kang and S. X. Dou, *J. Am. Chem. Soc.*, 2011, **133**, 19314–19317.
8 J. Y. Shin, D. Samuelis and J. Maier, *Adv. Funct. Mater.*, 2011, **21**, 3464–3472.
9 C. Sun, S. Rajasekhara, J. B. Goodenough and F. Zhou, *J. Am. Chem. Soc.*, 2011, **133**, 2132–2135.
10 D. Teng, Y. Yu, P. Li, X. Bai and X. Yang, *RSC Adv.*, 2013, **3**, 14237–14240.
11 Y. Wu, Z. Wen and J. Li, *Adv. Mater.*, 2011, **23**, 1126–1129.
12 J. Jamnik and J. Maier, *Phys. Chem. Chem. Phys.*, 2003, **5**, 5215–5220.
13 J. Sanz, J. E. Iglesias, J. Soria, E. R. Losilla, M. A. G. Aranda and S. Bruque, *Chem. Mater.*, 1997, **9**, 996–1003.
14 S. T. Norberg, G. Svensson and J. Albertsson, *Acta Cryst.*, 2001, **C57**, 225–227.
15 K. E. Lipinska-Kalita, M. B. Kruger, S. Carlson and A. M. K. Andersen, *Physica B*, 2003, **337**, 221–229.
16 Z. Shi, Q. Wang, W. Ye, Y. Li and Y. Yang, *Micropor. Mesopor. Mater.*, 2006, **88**, 232–237.
17 H. Wang, K. Huang, Y. Zeng, S. Yang and L. Chen, *Electrochim. Acta*, 2007, **52**, 3280–3285.
18 C. Lai, W. Wang, J. Gao, Y. Wang, S. Ye, L. Li and C. Wang, *RSC Adv.*, 2013, **3**, 13137–13139.
19 P. Barpanda, S. I. Nishimura and A. Yamada, *Adv. Energy Mater.,* 2012, **2**, 841–859.
20 R. A. Shakoor, H. Kim, W. Cho, S. Y. Lim, H. Song, J. W. Lee, J. K. Kang, Y. T. Kim, Y. Jung and J. W. Choi, *J. Am. Chem. Soc.*, 2012, **134**, 11740–11748.
21 I. C. Marcu, I. Sandulescu and J. M. M. Millet, *J. Mol. Catal. A: Chem.*, 2003, **203**, 241–250.
22 A. Muto, K. Ida, T. Bhaskar, M. A. Uddin, S. Takashima, T. Hirai and Y. Sakata, *Appl. Catal. A: Gen.*, 2004, **260**, 163–168.
23 V. Aravindan, M. V. Reddy, S. Madhavi, S. G. Mhaisalkar, G. V. Subba Rao and B. V. R. Chowdari, *J. Power Sources*, 2011, **196**, 8850–8854.
24 S. Patoux and C. Masquelier, *Chem. Mater.*, 2002, **14**, 5057–5068.
25 Y. Uebou, S. Okada, M. Egashira and J. I. Yamaki, *Solid State Ionics*, 2002, **148**, 323–328.
26 L. Chen, Q. Gu, X. Zhou, S. Lee, Y. Xia and Z. Liu, *Sci. Rep.*, 2013, **3**, 1946, doi: 10.1038/srep01946.

27 A. K. Padhhi, K. S. Nanjundaswamy and J. B. Goodenough, *J. Electrochem. Soc.*, 1997, **144**, 1188–1194.
28 S. Patoux, C. Bourbon, *US Pat.*, 7 879 264 B2, 1/2, 2011.
29 V. Nalini, M. H. Sørby, K. Amezawa, R. Haugsrud, H. Fjellvåg and T. Norby, *J. Am. Ceram. Soc.*, 2011, **94**, 1514–1522.
30 M. Armand and J. M. Tarascon, *Nature*, 2008, **451**, 652–657.
31 S. W. Oh, S. T. Myung, S. M. Oh, K. H. Oh, K. Amine, B. Scrosati and Y. K. Sun, *Adv. Mater.*, 2010, **22**, 4842–4845.
32 C. Y. Cummings, A. H. Roweth, A. K. Z. Ching , A. T. A. Jenkins, J. M. Mitchels, S. Shariki, S. Y. Liew, W. Thielemans, D. A. Walsh and F. Marken, *Electrochem. Commun.*, 2010, **12**, 1722–1726.
33 C. Bretti, R. M. Cigala, G. Lando, D. Milea and S. Sammartano, *J. Agric. Food Chem.*, 2012, **60**, 8075–8082.
34 U. Ulusoy, S. Şimşek and Ö. Ceyhan, *Adsorption*, 2003, **9**, 165–175.
35 J. Su, X. L. Wu, C. P. Yang, J. S. Lee, J. Kim and Y. G. Guo, *J. Phys. Chem. C*, 2012, **116**, 5019–5024.
36 J. Lehrfeld, *J. Agric. Food Chem.*, 1994, **42**, 2726–2731.
37 S. Loridant, I. C. March, G. Bergeret and J. M. M. Millet, *Phys. Chem. Chem. Phys.*, 2003, **5**, 4384–4389.
38 A. C. Ferrari and J. Robertson, *Phys. Rev. B*, 2000, **61**, 14095–14107.
39 V. Aravindan, W. Chuiling, M. V. Reddy, G. V. Subba Rao, B. V. R. Chowdari and S. Madhavi, *Phys. Chem. Chem. Phys.*, 2012, **14**, 5808–5814.
40 S. Zhu, Z. Wang, C. He, N. Zhao, C. Shi, E. Liu and J. Li, *J. Mater. Chem. A*, 2013, **1**, 11011–11018.
41 X. Fan, C. Yu, Z. Ling, J. Yang and J. Qiu, *ACS Appl. Mater. Interfaces*, 2013, **5**, 2104–2110.
42 Y. W. Xiao, J. Y. Lee, A. S. Yu and Z. L. Liu, *J. Electrochem. Soc.*, 1999, **146**, 3623–3629.
43 D. Guo, J. Mi, G. Hao, W. Dong, G. Xiong, W. Li and A. Lu, *Energy Environ. Sci.*, 2013, **6**, 652–659.
44 J. Y. Luo and Y. Y. Xia, *Adv. Funct. Mater.*, 2007, **17**, 3877–3884.
45 Z. Chen and J. R. Dahn, *J. Electrochem. Soc.*, 2002, **149**, A1184–A1189.
46 L. Ratke, P. W. Woorhees, *Growth and coarsening: Ostwald ripening in material processing*, Springer, 2002, pp. 117–118.
47 S. Bruque, M. A. G. Aranda, E. R. Losilla, P. Olivera-Pastor and P. Maireles-Torres, *Inorg. Chem.*, 1995, **34**, 893–899.
48 J. Yang, C. Xue, S. H. Yu, J. H. Zeng and Y. T. Qian, *Angew. Chem. Int. Ed.*, 2002, **41**, 4697–4700.
49 H. Zhang, R. Wu, Z. Chen, G. Liu, Z. Zhang and Z. Jiao, *CrystEngComm*, 2012, **14**, 1775–1782.
50 S. Amelinckx, X. B. Zhang, D. Bernaerts, X. F. Zhang, V. Ivanov and J. B. Nagy, *Science*, 1994, **265**, 635–639.
51 K. S. W. Sing, D. H. Everett, R. A. W. Haul, L. Moscou, R. A. Pierotti, J. Rouquérol and T. Siemieniewska, *Pure Appl. Chem.*, 1985, **57**, 603–619.
52 J. Yu, H. Yu, B. Cheng, M. Zhou and X. Zhao, *J. Mol. Catal. A: Chem.*, 2006, **253**, 112–118.
53 J. Niu, A. Kushima, X. Qian, L. Qi, K. Xiang, Y. M. Chiang, J. Li, Nano Lett., 2014, 14, 4005–4010.
54 G. Sudant, E. Baudrin, D. Larcher and J. M. Terascon, *J. Mater. Chem.*, 2005, **15**, 1263–1269.
55 M. Latorre-Sanhcez, A. Primo and H. Garcia, *J. Mater. Chem.*, 2012, **22**, 21373–21375.
56 X. L. Wu, L. Y. Jiang, F. F. Cao, Y. G. Guo and L. J. Wan, *Adv. Mater.*, 2009, **21**, 2710–2714.
57 C. He, S. Wu, N. Zhao, C. Shi, E. Liu and J. Li, *ACS Nano*, 2014, **7**, 4459–4469.
58 P. Wang, M. Gao, H. Pan, J. Zhang, C. Liang, J. Wang, P. Zhou and Y. Liu, *J. Power Sources*, 2013, **239**, 466–474.
59 S. Jin, H. Deng, D. Long, X. Liu, L. Zhan, X. Liang, W. Qiao and L. Ling, *J. Power Sources*, 2011, **196**, 3887–3893.
60 Y. G. Guo, Y. S. Hu and J. Maier, *Chem. Commun.*, 2006, 2783–2785.
61 Y. F. Wu, Y. N. Liu, S. W. Guo, S. N. Zhang, T. N. Lu, Z. M. Yu, C. S. Li and Z. P. Xi, *J. Power Sources*, 2014, **256**, 336–344.
62 A. J. Bard, L. R. Faulkner, *Electrochemical methods: fundamentals and applications*, Wiley, New York, 2nd edn., 1980, pp. 231–232.

Table of contents entry

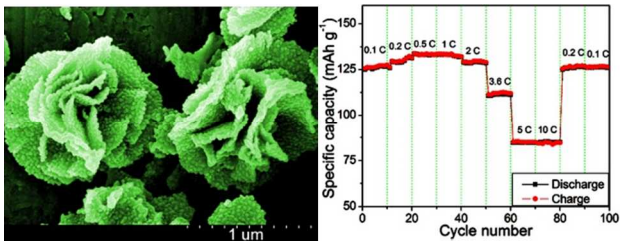

Polyhierarchically structured TiP_2O_7/C microparticles constructed by carbon-coated nanoflakes enchasing crystalline nanoparticles have been prepared by directly annealing flower-like titanium hydrogen phosphate hydrate ($Ti(HPO_4)_2 \cdot xH_2O$) microparticles, and exhibit enhanced electrochemical performance attributed to interfacial Li-storage and fast Li-ion diffusion due to the polyhierarchical architecture with carbon nano-coating and 3D open pores.